Science Advances
AAAS

Supplementary Materials for

Resolving the molecular architecture of the photoreceptor active zone with 3D-MINFLUX

Chad P. Grabner *et al.*

Corresponding author: Chad P. Grabner, chadgrabner@gmail.com; Christian A. Wurm, c.wurm@abberior-instruments.com; Tobias Moser, tmoser@gwdg.de

Sci. Adv. **8**, eabl7560 (2022)
DOI: 10.1126/sciadv.abl7560

The PDF file includes:

Other Supplementary Material for this manuscript includes the following:

Supplementary Materials and Figures

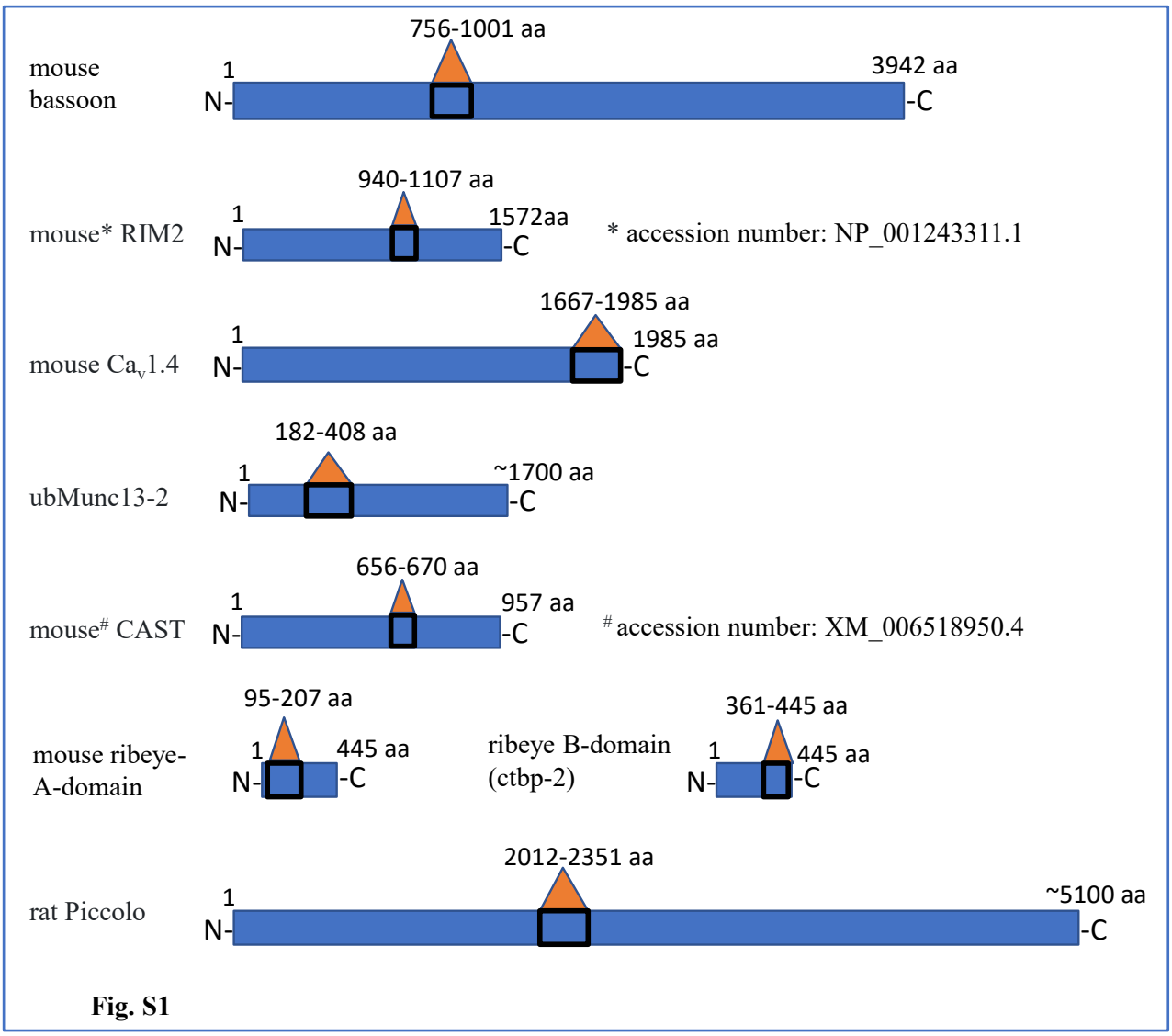

Fig. S1

figure S1. Schematic of epitopes used to create antibodies against the AZ proteins used in this study. Antibodies designed against CAST and RIM2 were based on protein amino acid (a.a.) sequences from rat as presented in Table1; however, in this figure the aa sequences for mouse RIM2 and CAST are presented. The database (accession number) used for mouse a.a. sequences are indicated in the figure. See Table one for details on antibody sources and references.

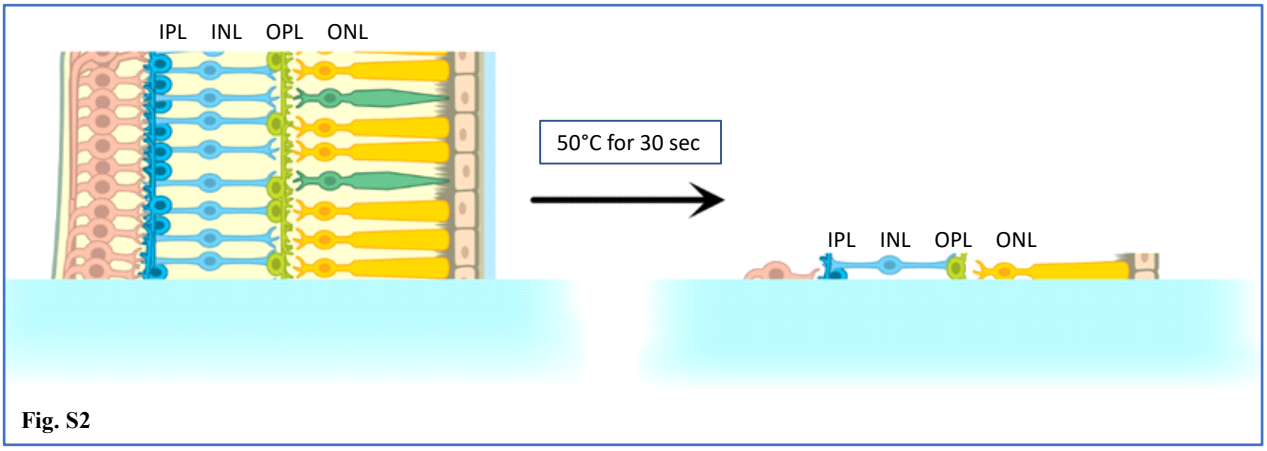

Fig. S2

figure S2. Illustration of how retinal tissue is transferred to glass using Heat Assisted Rapid Dehydration (HARD)**.** A slice of retina, made by cutting vertical sections through flat-mounted retina, is shown positioned on a glass coverslip. The coverslip was pre-warmed to 50°C prior to applying the slice. Once the slice contacted the glass, it was held in place for 30 sec and then retracted. A thin layer of the slice is shown to remain on the glass. The coverslip was left on the thermal plate for 2 to 5 minutes to ensure complete dehydration.

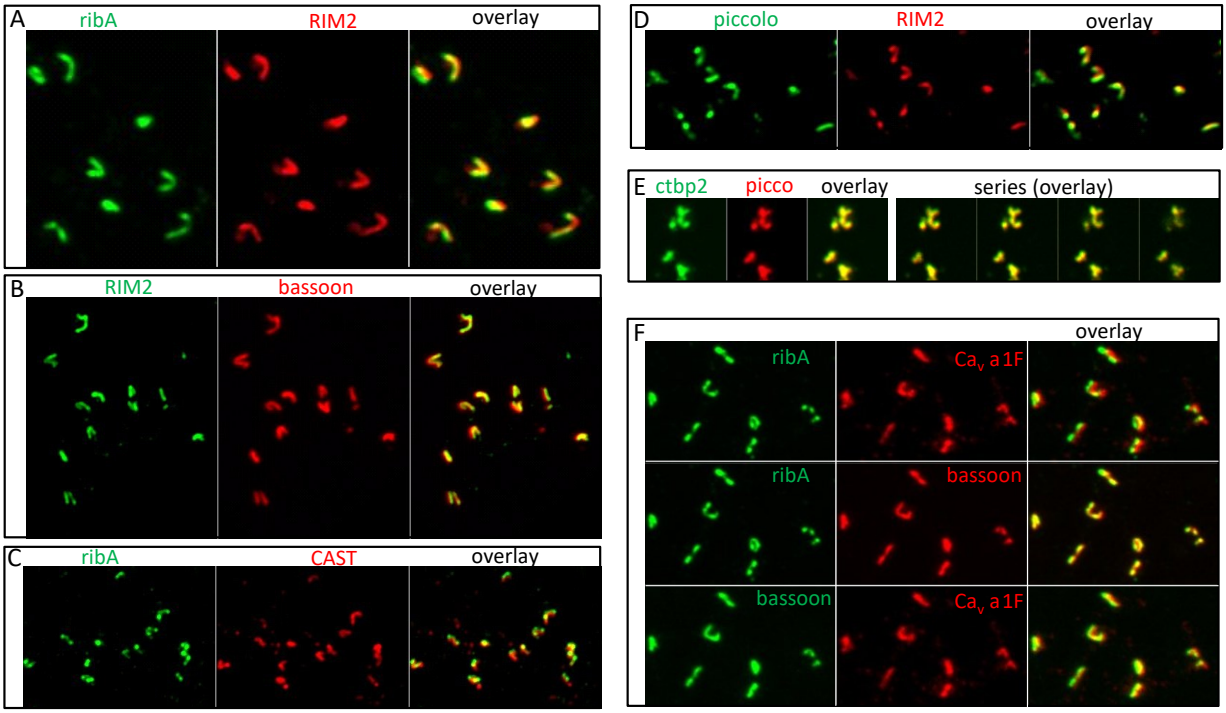

Fig. S3

figure S3. Confocal images of rod terminals in HARD samples exhibit the normal colocalization of synaptic ribbon and active zone markers. (**A**) RIM2 (red, Alexa647) co-stained with ribbon marker ribA (= ribeye A-domain; green, Alexa488). (**B**) RIM2 (green, Alexa488) active zone marker bassoon (red, Alexa647). (**C**) Co-labeling of ribA (green, Alexa488) with active zone protein CAST (red, Alexa647). (**D**) Co-staining of piccolo (green, Alexa488) and RIM2 (red, Alexa647). (**E**) Illustrates the complete overlap of the two ribbon markers piccolo (red, Alexa647) and ctpb2 (ribeye B-domain; green, Alexa488). (**F**) Presents the co-labeling of Ca_v channel pore forming subunit α1F (Alexa647) against ribA (Alexa488) and bassoon (Alexa546).

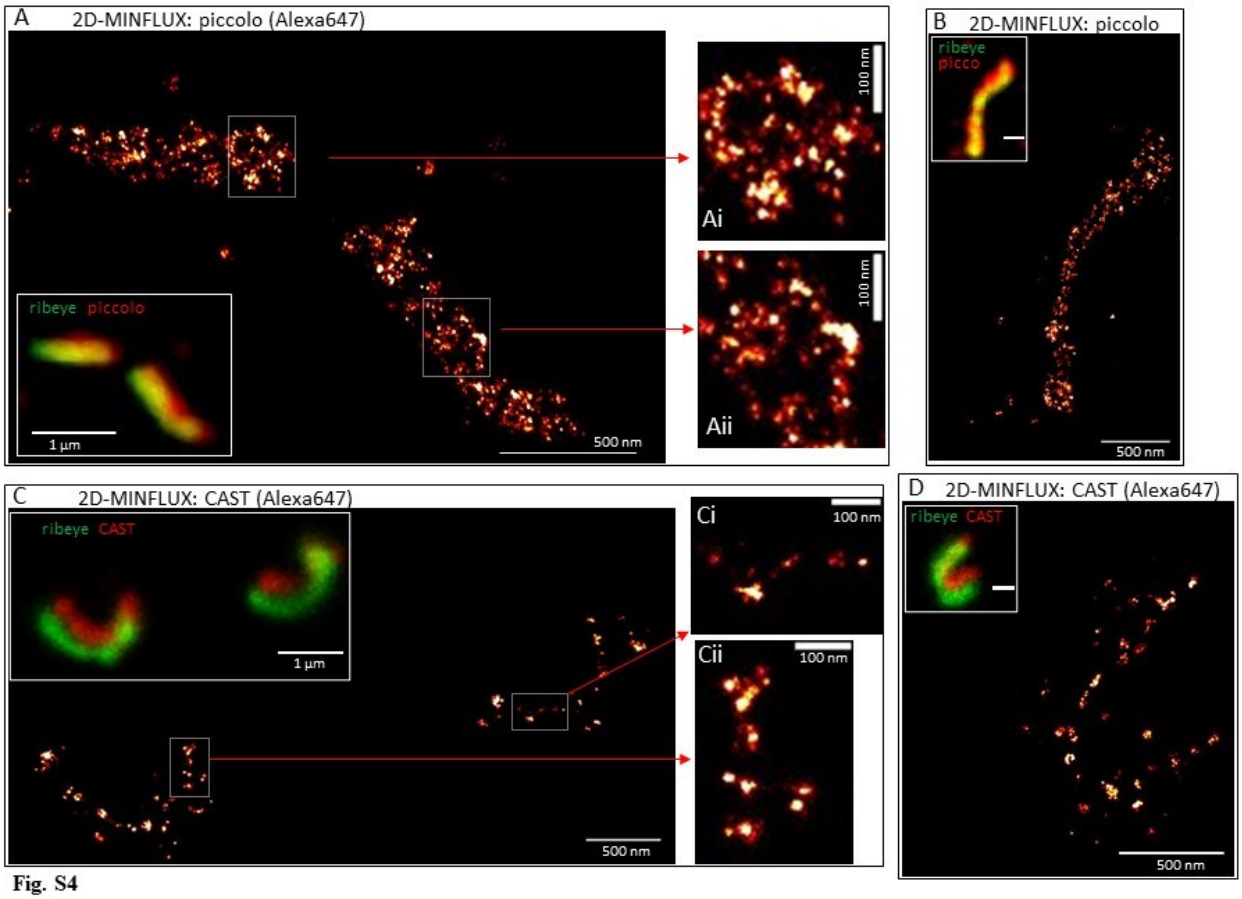

Fig. S4

figure S4. 2D-MINFLUX localizations for piccolo and CAST. (**A** and **B**) Insets show confocal images of rod ribbons indirectly labelled for piccolo (red, Alexa647) and ribeye (green, Alexa488). The two proteins are highly colocalized. 2D-MINFLUX images of piccolo are presented on full scale in (A) and (B). Highlighted regions of interest presented in (**Ai, ii**) show the dense mesh of piccolo localizations. Confocal inset in (B) has a scale bar = 500 nm. (**C** and **D**) Inset present confocal images of rod ribbons indirectly labelled for CAST (red, Alexa647) and ribeye (green, Alexa488). Co-localization is minimal, especially when compared to piccolo. 2D-MINFLUX images of CAST are presented on full scale in (C) and (D) and show lower labeling density than what is observed for piccolo. Highlighted regions of interest presented in (**Ci, ii**) show a linear band of CAST, and a couple localizations displaced from the band. Scale bar = 500 nm in confocal inset in (D).

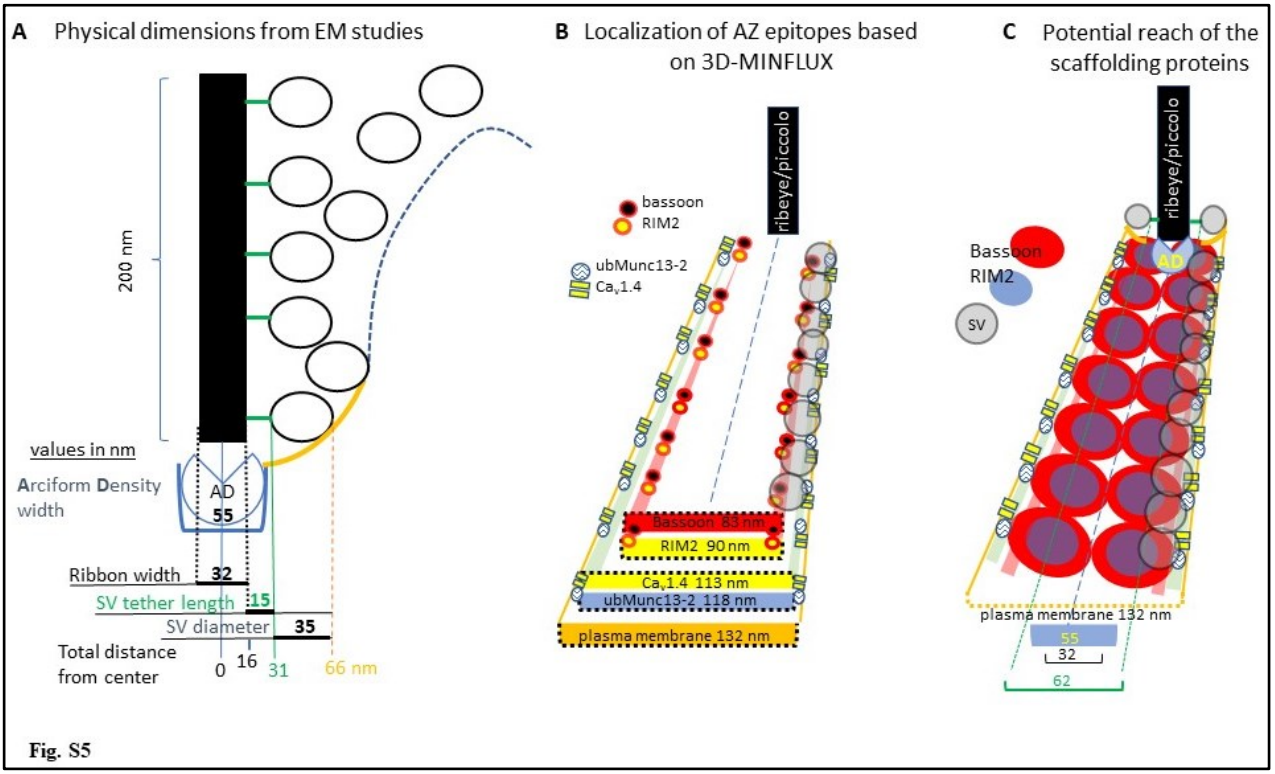

Fig. S5

figure S5. Proposed model of the molecular topography of the rod ribbon active zone. (**A**) Schematic representations of the base of the rod ribbon AZ. Taking the point where the SV contacts the plasma membrane as a SV release site, then the upper estimate for the distance between the center/midline of the ribbon to the SV at the base is 66 nm. Values present in the schematic are in nanometers, and they are taken from published electron microscopy studies (*25*, *29*, *32*, *57*). **(B)** Summary of 3D-MINFLUX results. The distance between the "plasma membrane" release sites is 132 nm (2 × 66 nm). The distances between the two rows of AZ epitopes are given for each protein. Since the spacing between rows of $Ca_V1.4$ and ubMunc13-2 were not statistically different, they were grouped together, and for the same reason the scaffolding proteins RIM2 and bassoon were grouped together. Rows of $Ca_V1.4$ and ubMunc13-2 were significantly separated from the scaffolding proteins (see Results). The right half of the schematic includes SVs. **C**. The outlines of the ribbon AZ (from A) are overlaid with the AZ proteins. In addition, the compactness of the AZ proteins is incorporated into the illustration. Since $Ca_V1.4$ and ubMunc13-2 are likely more compact than the scaffolding proteins, and not likely to extend much beyond the location of the epitopes, they are given a compact representation in (C) and (B). In contrast the scaffolding proteins are less compact and may reach beyond the uncertainty inherent in the localization of their epitopes with the indirect antibody labeling procedure (~10 nm); therefore, the scaffolding proteins are

represented by a larger area of uncertainty. For example, bassoon is over twice the molecular weight of RIM2 and it is predicted to have a length of 80 nm in silico (*34*).

Supplemental Materials: HARD samples

As described in the Results, initial attempts at 2D-MINFLUX failed because of excessively high rates of photon emission. Both the density of ribbons per unit volume in the OPL, out of focus ribbons, and a large copy number of ribeye molecules per ribbon contributed to the excessive rates of photon emissions. To overcome these obstacles the next cycle of optimization made two distinct changes. First, rather than attempt to reduce emission density by lowering labelling efficiency (for example, lower primary and/or secondary antibody concentrations), or by suppressing emission rates per fluorophore by increasing the concentration of sulfhydryl compounds (e.g., β-mercaptoethanol) that suppress fluorophore blinking, AZ proteins (such as, RIM2) were targeted since they are presumed to be expressed at a lower copy number than ribeye. Second, to further reduce emission density from ribbon crowding in the OPL, a new approach was designed to deposit a thin layer of retinal slice on a standard glass coverslip. In addition, aldehydes were omitted to avoid increasing autofluorescence and degradation of AZ protein epitopes.

HARD sample rationale and development

Sample dehydration is commonly used during the processing of samples for conventional electron microscopy (EM) and immuno-fluorescence (IF) imaging. This often involves use of ethanol or methanol to remove water from the tissue (dehydrate) when making samples for EM. IF methods use alcohols to denature proteins so that they are rendered immobile, and in some instances the alcohol concentration may be high enough to dehydrate the tissue (*33*). Two procedures of interest either evacuate water under vacuum (*58*), or evaporate water from thin sections of retina through warming that samples (*32*, *59*). For instance, a standard approach used for preparing retinal samples for IF entails making cryo-sections from whole eyes frozen to a temperature of −20ºC, or less. Freshly cut frozen sections have a thickness of 15 to 20 μm, and they are transferred directly onto glass slides that are at a temperature of ~23°C. The glass slides are then placed on a thermal plate that is preheated to 50ºC and allowed to warm up for 10 minutes, which dehydrates the tissue (*32*). This procedure immobilizes large AZ proteins at rod ribbons in the OPL, and has the benefit of not requiring aldehyde fixation; however, smaller cytosolic proteins may require aldehyde fixation to retain them in the tissue (*32*). When aldehyde fixation is required, it can create a noticeable increase in background signal (noise), and diminish the target protein's epitope (*32*, *33*). Hence, the standard dehydration method used with cryosections, and the more advanced vacuum dehydration approach, give improved labeling when aldehydes are omitted.

Assuming dehydration, and denaturation, were the critical events that rendered the AZ proteins fixed in the different protocols outlined above, it was reasoned that it may be possible to avoid the freezing step and go directly to dehydrating the retinal tissue. To do this, a living retinal slice attached to a piece of nitrocellulose membrane was taken out of solution, and excess solution carried on the forceps and nitrocellulose membrane were drawn off with a small piece of Kimwipe tissue paper. The slice was oriented as indicated in figure S1 and placed gently onto a glass coverslip prewarmed to 50ºC on a thermal plate. After 20 to 30 sec the slice was withdrawn from the glass. A thin layer of tissue remained on the glass and appeared translucent for ~1 sec prior to becoming grey and dehydrated. The coverslip was left on the thermal plate for a couple more minutes. After this, coverslips were stored at room temperature in a desiccated chamber for up to 2 weeks. Validation of the samples for IF is documented in the Results (Fig. 1-3, fig. S3; movies: 1-6), and the immune-staining procedure is outlined in the Methods section.

Additional technical notes. The reason for withdrawing the slice is that we did not want a thick layer of retina (the retinal slices on nitrocellulose paper are between 150 to 200 μm in thickness), which would cause excessive out-of-focus signal. In addition, a thin layer of retina will dehydrate faster, and withdrawing the slice leaves a thin layer of tissue on the glass that dehydrates rapidly. To optimize the procedure, excess liquid had to be removed from the slices for two reasons. First, it was desired to have the retinal slice warm rapidly (from ~23°C to 50ºC, ΔT ~27ºC), and excess solution consumes heat that would otherwise be transferred to the retinal slice. Second, the final step aimed to dehydrate the tissue as fast as possible, after the slice was withdrawn, and the presence of excess solution would prolong the dehydration step. If excess solution was not removed, then a residual bead of solution was left on the glass coverslip after the retinal slice was removed. Once the water evaporated the appearance was not a clean imprint of the slice, but rather a salt residue remained.

Movie Captions.

Movie 1. Confocal stack (320 nm thick sections) made through the OPL of a fixed retinal slice labelled with anti-ctbp2 (ribeye B-domain) using conventional methods (fixed with 3 % PFA and detergent permeabilized).

Movie 2. HARD retinal sample stained for ubMunc13-2 (red) and ribeye-A (green). Confocal optical sections taken at a thickness of 1 micron.

Movie 3. Retinal HARD sample stained for ubMunc13-2 (red) and ribeye-A (green). Zoomed in view of photoreceptors in the OPL. 200 nm optical sections.

Movie 4. Shows a series of optical sections through terminals bounded by vglut1 (green). The red channel presents bassoon + RIM2.

Movie 5. Red channel presents bassoon + RIM2.

Movie 6. Brightfield image with an overlay of bassoon and RIM2 (both in the red channel).

Movie 7. Bassoon 3D-MINFLUX. Color-coded, depth heat map. Edge of square = 100 nm.

Movie 8. Bassoon 3D-MINFLUX. Grey scale. Edge of square = 100 nm.

Movie 9. RIM2 3D-MINFLUX. Color-coded, depth heat map. Edge of square = 100 nm.

Movie 10. RIM2 3D-MINFLUX. Grey scale. Edge of square = 100 nm.

Movie 11. ubMunc13-2 3D-MINFLUX. Color-coded, depth heat map. Edge of square = 100 nm.

Movie 12. ubMunc13-2 3D-MINFLUX. Grey scale. Edge of square = 100 nm.

Movie 13. Cav1.4-a1F 3D-MINFLUX. Color-coded, depth heat map. Edge of square = 100 nm.

Movie 14. Cav1.4-a1F 3D-MINFLUX. Grey scale. Edge of square = 100 nm.

REFERENCES AND NOTES

1. J. E. Heuser, T. S. Reese, M. J. Dennis, Y. Jan, L. Jan, L. Evans, Synaptic vesicle exocytosis captured by quick freezing and correlated with quantal transmitter release. *J. Cell Biol.* **81**, 275–300 (1979).

2. M. L. Harlow, D. Ress, A. Stoschek, R. M. Marshall, U. J. McMahan, The architecture of active zone material at the frog's neuromuscular junction. *Nature* **409**, 479–84 (2001).

3. J. H. Jung, J. A. Szule, R. M. Marshall, U. J. McMahan, Variable priming of a docked synaptic vesicle. *Proc. Natl. Acad. Sci. U.S.A.* **113**, E1098–E1107 (2016).

4. C. Limbach, M. M. Laue, X. Wang, B. Hu, N. Thiede, G. Hultqvist, M. W. Kilimann, Molecular in situ topology of Aczonin/Piccolo and associated proteins at the mammalian neurotransmitter release site. *Proc. Natl. Acad. Sci.* **108**, E392–E401 (2011).

5. N. Holderith, A. Lorincz, G. Katona, B. Rózsa, A. Kulik, M. Watanabe, Z. Nusser, Release probability of hippocampal glutamatergic terminals scales with the size of the active zone. *Nat. Neurosci.* **15**, 988–997 (2012).

6. N. Brose, A. Brunger, D. Cafiso, E. R. Chapman, J. Diao, F. M. Hughson, M. B. Jackson, R. Jahn, M. Lindau, C. Ma, J. Rizo, Y. K. Shin, T. H. Sollner, L. Tamm, T. Y. Yoon, Y. Zhang, Synaptic vesicle fusion: Today and beyond. *Nat. Struct. Mol. Biol.* **26**, 663–668 (2019).

7. H. Sakamoto, T. Ariyoshi, N. Kimpara, K. Sugao, I. Taiko, K. Takikawa, D. Asanuma, S. Namiki, K. Hirose, Synaptic weight set by Munc13-1 supramolecular assemblies. *Nat. Neurosci.* **21**, 41–49 (2018).

8. J. Neef, N. T. Urban, T.-L. Ohn, T. Frank, P. Jean, S. W. Hell, K. I. Willig, T. Moser, Quantitative optical nanophysiology of Ca^{2+} signaling at inner hair cell active zones. *Nat. Commun.* **9**, 290 (2018).

9. N. Ehmann, S. van de Linde, A. Alon, D. Ljaschenko, X. Z. Keung, T. Holm, A. Rings, A. DiAntonio, S. Hallermann, U. Ashery, M. Heckmann, M. Sauer, R. J. Kittel, Quantitative

super-resolution imaging of Bruchpilot distinguishes active zone states. *Nat. Commun.* **5**, 4650 (2014).

10. M. Klevanski, F. Herrmannsdoerfer, S. Sass, V. Venkataramani, M. Heilemann, T. Kuner, Automated highly multiplexed super-resolution imaging of protein nano-architecture in cells and tissues. *Nat. Commun.* **11**, 1552 (2020).

11. M. A. Böhme, C. Beis, S. Reddy-Alla, E. Reynolds, M. M. Mampell, A. T. Grasskamp, J. Lützkendorf, D. D. Bergeron, J. H. Driller, H. Babikir, F. Göttfert, I. M. Robinson, C. J. O'Kane, S. W. Hell, M. C. Wahl, U. Stelzl, B. Loll, A. M. Walter, S. J. Sigrist, Active zone scaffolds differentially accumulate Unc13 isoforms to tune Ca^{2+} channel–vesicle coupling. *Nat. Neurosci.* **19**, 1311–1320 (2016).

12. F. Balzarotti, Y. Eilers, K. C. Gwosch, A. H. Gynnå, V. Westphal, F. D. Stefani, J. Elf, S. W. Hell, Nanometer resolution imaging and tracking of fluorescent molecules with minimal photon fluxes. *Science* **355**, 606–612 (2017).

13. R. Schmidt, T. Weihs, C. A. Wurm, I. Jansen, J. Rehman, S. J. Sahl, S. W. Hell, MINFLUX nanometer-scale 3D imaging and microsecond-range tracking on a common fluorescence microscope. *Nat. Commun.* **12**, 1478 (2021).

14. P. Jean, D. Lopez de la Morena, S. Michanski, L. M. Jaime Tobón, R. Chakrabarti, M. M. Picher, J. Neef, S. Jung, M. Gültas, S. Maxeiner, A. Neef, C. Wichmann, N. Strenzke, C. Grabner, T. Moser, The synaptic ribbon is critical for sound encoding at high rates and with temporal precision. *eLife* **7**, e29275 (2018).

15. S. Maxeiner, F. Luo, A. Tan, F. Schmitz, T. C. Südhof, How to make a synaptic ribbon: RIBEYE deletion abolishes ribbons in retinal synapses and disrupts neurotransmitter release. *EMBO J.* **35**, 1098–1114 (2016).

16. T. Vaithianathan, D. Henry, W. Akmentin, G. Matthews, Nanoscale dynamics of synaptic vesicle trafficking and fusion at the presynaptic active zone. *eLife* **5**, e13245 (2016).

17. T. Moser, C. P. Grabner, F. Schmitz, Sensory processing at ribbon synapses in the retina and the cochlea. *Physiol. Rev.* **100**, 103–144 (2019).

18. W. B. Thoreson, K. Rabl, E. Townes-Anderson, R. Heidelberger, A highly Ca^{2+}-sensitive pool of vesicles contributes to linearity at the rod photoreceptor ribbon synapse. *Neuron* **42**, 595–605 (2004).

19. F. Rieke, E. A. Schwartz, Asynchronous transmitter release: Control of exocytosis and endocytosis at the salamander rod synapse. *J. Physiol.* **493**, 1–8 (1996).

20. M. Chen, M. J. V. Hook, D. Zenisek, W. B. Thoreson, Properties of ribbon and non-ribbon release from rod photoreceptors revealed by visualizing individual synaptic vesicles. *J. Neurosci.* **33**, 2071–2086 (2013).

21. C. P. Grabner, T. Moser, The mammalian rod synaptic ribbon is essential for Ca_v channel facilitation and ultrafast synaptic vesicle fusion. *eLife* **10**, e63844 (2021).

22. D. Zenisek, N. K. Horst, C. Merrifield, P. Sterling, G. Matthews, Visualizing synaptic ribbons in the living cell. *J. Neurosci.* **24**, 9752–9759 (2004).

23. F. Schmitz, A. Königstorfer, T. C. Südhof, RIBEYE, a component of synaptic ribbons: A protein's journey through evolution provides insight into synaptic ribbon function. *Neuron* **28**, 857–872 (2000).

24. V. Kerov, J. G. Laird, M. Joiner, S. Knecht, D. Soh, J. Hagen, S. H. Gardner, W. Gutierrez, T. Yoshimatsu, S. Bhattarai, T. Puthussery, N. O. Artemyev, A. V. Drack, R. O. Wong, S. A. Baker, A. Lee, α2δ-4 is required for the molecular and structural organization of rod and cone photoreceptor synapses. *J. Neurosci.* **38**, 6145–6160 (2018).

25. B. Cooper, M. Hemmerlein, J. Ammermuller, C. Imig, K. Reim, N. Lipstein, S. Kalla, H. Kawabe, N. Brose, J. H. Brandstatter, F. Varoqueaux, Munc13-independent vesicle priming at mouse photoreceptor ribbon synapses. *J. Neurosci.* **32**, 8040–8052 (2012).

26. A. Hagiwara, Y. Kitahara, C. P. Grabner, C. Vogl, M. Abe, R. Kitta, K. Ohta, K. Nakamura, K. Sakimura, T. Moser, A. Nishi, T. Ohtsuka, Cytomatrix proteins CAST and ELKS regulate retinal photoreceptor development and maintenance. *J. Cell Biol.* **217**, 3993–4006 (2018).

27. D. Khimich, R. Nouvian, R. Pujol, Susanne tom Dieck, A. Egner, E. D. Gundelfinger, T. Moser, Hair cell synaptic ribbons are essential for synchronous auditory signalling. *Nature* **434**, (2005).

28. S. Michanski, K. Smaluch, A. M. Steyer, R. Chakrabarti, C. Setz, D. Oestreicher, C. Fischer, W. Möbius, T. Moser, C. Vogl, C. Wichmann, Mapping developmental maturation of inner hair cell ribbon synapses in the apical mouse cochlea. *Proc. Natl. Acad. Sci. U.S.A.* **116**, 6415–6424 (2019).

29. T. M. Müller, K. Gierke, A. Joachimsthaler, H. Sticht, Z. Izsvák, F. K. Hamra, A. Fejtová, F. Ackermann, C. C. Garner, J. Kremers, J. H. Brandstätter, H. Regus-Leidig, A multiple piccolino-RIBEYE interaction supports plate-shaped synaptic ribbons in retinal neurons. *J. Neurosci.* **39**, 2606–2619 (2019).

30. M. Deguchi-Tawarada, E. Inoue, E. Takao-Rikitsu, M. Inoue, I. Kitajima, T. Ohtsuka, Y. Takai, Active zone protein CAST is a component of conventional and ribbon synapses in mouse retina. *J. Comp. Neurol.* **495**, 480–496 (2006).

31. S. tom Dieck, W. D. Altrock, M. M. Kessels, B. Qualmann, H. Regus, D. Brauner, A. Fejtová, O. Bracko, E. D. Gundelfinger, J. H. Brandstätter, Molecular dissection of the photoreceptor ribbon synapse physical interaction of Bassoon and RIBEYE is essential for the assembly of the ribbon complex. *J. Cell Biol.* **168**, 825–836 (2005).

32. C. P. Grabner, M. A. Gandini, R. Rehak, Y. Le, G. W. Zamponi, F. Schmitz, RIM1/2-mediated facilitation of Cav1.4 channel opening is required for Ca^{2+}-stimulated release in mouse rod photoreceptors. *J. Neurosci.* **35**, 13133–13147 (2015).

33. T. W. Stradleigh, A. T. Ishida, Fixation strategies for retinal immunohistochemistry. *Prog. Retin. Eye Res.* **48**, 181–202 (2015).

34. E. D. Gundelfinger, C. Reissner, C. C. Garner, Role of bassoon and piccolo in assembly and molecular organization of the active zone. *Front. Synaptic Neurosci.* **7**, 19 (2016).

35. A. Brandt, Few $Ca_V1.3$ channels regulate the exocytosis of a synaptic vesicle at the hair cell ribbon synapse. *J. Neurosci.* **25**, 11577–11585 (2005).

36. C. W. Graydon, S. Cho, G.-L. Li, B. Kachar, H. von Gersdorff, Sharp Ca2+ nanodomains beneath the ribbon promote highly synchronous multivesicular release at hair cell synapses. *J. Neurosci.* **31**, 16637–16650 (2011).

37. W. M. Roberts, R. A. Jacobs, A. J. Hudspeth, Colocalization of ion channels involved in frequency selectivity and synaptic transmission at presynaptic active zones of hair cells. *J. Neurosci.* **10**, 3664–3684 (1990).

38. T. Jarsky, M. Tian, J. H. Singer, Nanodomain control of exocytosis is responsible for the signaling capability of a retinal ribbon synapse. *J. Neurosci.* **30**, 11885–11895 (2010).

39. R. Rao-Mirotznik, A. B. Harkins, G. Buchsbaum, P. Sterling, Mammalian rod terminal: Architecture of a binary synapse. *Neuron* **14**, 561–569 (1995).

40. B. Beckwith-Cohen, L. C. Holzhausen, T.-M. Wang, R. Rajappa, R. H. Kramer, Localizing proton-mediated inhibitory feedback at the retinal horizontal cell–cone synapse with genetically-encoded pH probes. *J. Neurosci.* **39**, 651–662 (2019).

41. R. Rao-Mirotznik, G. Buchsbaum, P. Sterling, Transmitter concentration at a three-dimensional synapse. *J. Neurophysiol.* **80**, 3163–3172 (1998).

42. M. C. van Rossum, R. G. Smith, Noise removal at the rod synapse of mammalian retina. *Vis. Neurosci.* **15**, 809–821 (1998).

43. N. M. Chapochnikov, H. Takago, C.-H. Huang, T. Pangršič, D. Khimich, J. Neef, E. Auge, F. Göttfert, S. W. Hell, C. Wichmann, F. Wolf, T. Moser, Uniquantal release through a dynamic fusion pore is a candidate mechanism of hair cell exocytosis. *Neuron* **83**, 1389–1403 (2014).

44. A. B. Wong, M. A. Rutherford, M. Gabrielaitis, T. Pangršič, F. Göttfert, T. Frank, S. Michanski, S. Hell, F. Wolf, C. Wichmann, T. Moser, Developmental refinement of hair cell synapses tightens the coupling of Ca^{2+} influx to exocytosis. *EMBO J.* **33**, 247–264 (2014), doi:10.1002/embj.201387110.

45. T. Pangršič, M. Gabrielaitis, S. Michanski, B. Schwaller, F. Wolf, N. Strenzke, T. Moser, EF-hand protein Ca^{2+} buffers regulate Ca^{2+} influx and exocytosis in sensory hair cells. *Proc. Natl. Acad. Sci. U.S.A.* **112**, E1028–E1037 (2015).

46. H. Hibino, R. Pironkova, O. Onwumere, M. Vologodskaia, A. J. Hudspeth, F. Lesage, RIM binding proteins (RBPs) couple Rab3-interacting molecules (RIMs) to voltage-gated Ca2+ channels. *Neuron* **34**, 411–423 (2002).

47. T. Butola, T. Alvanos, A. Hintze, P. Koppensteiner, D. Kleindienst, R. Shigemoto, C. Wichmann, T. Moser, RIM-binding protein 2 organizes Ca2+ channel topography and regulates release probability and vesicle replenishment at a fast central synapse. *J. Neurosci.* **41**, 7742–7767 (2021).

48. Y. Nakamura, H. Harada, N. Kamasawa, K. Matsui, J. S. Rothman, R. Shigemoto, R Angus Silver, D. A. Di Gregorio, T. Takahashi, Nanoscale distribution of presynaptic Ca^{2+} channels and its impact on vesicular release during development. *Neuron* **85,** 145–158 (2015).

49. K. C. Gwosch, J. K. Pape, F. Balzarotti, P. Hoess, J. Ellenberg, J. Ries, S. W. Hell, MINFLUX nanoscopy delivers 3D multicolor nanometer resolution in cells. *Nat. Methods* **17**, 217–224 (2020).

50. J. Ahrens, B. Geveci, C. Law, ParaView: An end-user tool for large data visualization. *Vis. Handb.* 717–731 (2005).

51. O. Dick, S. tom Dieck, W. D. Altrock, J. Ammermüller, R. Weiler, C. C. Garner, E. D. Gundelfinger, J. H. Brandstätter, The presynaptic active zone protein bassoon is essential for photoreceptor ribbon synapse formation in the retina. *Neuron* **37**, 775–786 (2003).

52. S. Jung, T. Oshima-Takago, R. Chakrabarti, A. B. Wong, Z. Jing, G. Yamanbaeva, M. M. Picher, S. M. Wojcik, F. Göttfert, F. Predoehl, K. Michel, S. W. Hell, S. Schoch, N. Strenzke C. Wichmann, T. Moser, Rab3-interacting molecules 2α and 2β promote the abundance of voltage-gated $Ca_V1.3$ Ca^{2+} channels at hair cell active zones. *Proc. Natl. Acad. Sci. U.S.A.* **112**, E3141–E3149 (2015).

53. M. Ryl, A. Urbasik, K. Gierke, N. Babai, A. Joachimsthaler, A. Feigenspan, R. Frischknecht N. Stallwitz, A. Fejtová, J. Kremers, J. von Wittgenstein, J. H. Brandstätter, Genetic disruption of bassoon in two mutant mouse lines causes divergent retinal phenotypes. *FASEB J.* **35**, e21520 (2021).

54. L. Klotz, O. Wendler, R. Frischknecht, R. Shigemoto, H. Schulze, R. Enz, Localization of group II and III metabotropic glutamate receptors at pre- and postsynaptic sites of inner hair cell ribbon synapses. *FASEB J.* **33**, 13734–13746 (2019).

55. J. Gehlen, C. Aretzweiler, A. Mataruga, C. Fahlke, F. Müller, Excitatory amino acid transporter EAAT5 improves temporal resolution in the retina. *eNeuro* **8**, ENEURO.0406-21.2021 (2021).

56. T. Butola, C. Wichmann, T. Moser, Piccolo promotes vesicle replenishment at a fast central auditory synapse. *Front. Synaptic Neurosci.* **9**, 14 (2017).

57. G. A. Zampighi, C. Schietroma, L. M. Zampighi, M. Woodruff, E. M. Wright, N. C. Brecha, Conical tomography of a ribbon synapse: Structural evidence for vesicle fusion. *PLOS ONE* **6**, e16911 (2011).

58. E. Dembla, M. Dembla, S. Maxeiner, F. Schmitz, Synaptic ribbons foster active zone stability and illumination-dependent active zone enrichment of RIM2 and Cav1.4 in photoreceptor synapses. *Sci. Rep.* **10**, 5957 (2020).

59. F. Schmitz, M. Bechmann, D. Drenckhahn, Purification of synaptic ribbons, structural components of the photoreceptor active zone complex, *J. Neurosci.* **16**, 7109–7116 (1996).